

Core-crown Quantum Nanoplatelets with Favorable Type-II Heterojunctions Boost Charge Separation and Photocatalytic NO Oxidation on TiO₂

Elnaz Ebrahimi,^[a] Muhammad Irfan,^[a, b] Farzan Shabani,^[c] Yusuf Kocak,^[a] Bartu Karakurt,^[a] Emre Erdem,^[d, e] Hilmi Volkan Demir,^[c, f, g] and Emrah Ozensoy*^[a, c]

Functionalization of TiO₂ (P25) with oleic acid-capped CdSe (core)/CdSeTe(crown) quantum-well nanoplatelets (NPL) yielded remarkable activity and selectivity toward nitrate formation in photocatalytic NO_x oxidation and storage (PHONOS) under both ultraviolet (UV-A) and visible (VIS) light irradiation. In the NPL/P25 photocatalytic system, photocatalytic active sites responsible for the NO(g) photo-oxidation and NO₂ formation reside mostly on titania, while the main function of the NPL is associated with the photocatalytic conversion of the generated NO₂ into the adsorbed NO₃⁻ species, significantly boosting

selectivity toward NO_x storage. Photocatalytic improvement in NO_x oxidation and storage upon NPL functionalization of titania can also be associated with enhanced electron-hole separation due to a favorable Type-II heterojunction formation and photo-induced electron transfer from the CdSeTe crown to the CdSe core of the quantum well system, where the trapped electrons in the CdSe core can later be transferred to titania. Re-usability of NPL/P25 system was also demonstrated upon prolonged use of the photocatalyst, where NPL/P25 catalyst surpassed P25 benchmark in all tests.

Introduction

Atmospheric pollution is one of the major environmental challenges faced by modern human society. Various anthropogenic air pollutants such as CO_x, SO_x, particulate matter (PM), volatile organic compounds (VOC), and nitrogen oxides (NO_x)

can contribute to acid rain and/or induce ozone (O₃) production in troposphere (*i.e.* unwanted ground-level ozone formation). In addition, human respiratory and immune systems are severely affected by nitric oxide (NO) and nitrogen dioxide (NO₂).^[1] Environmental protection agencies have set a value of ≤ 0.2 ppm for NO_x emissions but it is often exceeded in urban settings.^[2] Hence, it is crucial to find improved protocols for the removal of NO_x species from the atmosphere. Conventionally, NO_x abatement is typically performed at elevated temperatures (*e.g.* 200–550 °C) using thermal catalytic technologies (*e.g. via* selective catalytic reduction/SCR, NO_x storage and reduction/NSR, or three way catalysis/TWC)^[3–10] with an intend to curtail the toxic NO_x emissions at the source of generation. Frequent violations of transportation-based NO_x emission regulation^[11] necessitates the reduction of gaseous NO_x species after their point of origin under ambient conditions (*i.e.* at room temperature and under atmospheric pressure). It is important to note that, while all of these conventional catalytic DeNO_x technologies operate at the point of NO_x production (*i.e.* at the tailpipe or in the chimney *etc.*), there is no conventional catalytic DeNO_x technology that can be utilized after toxic NO_x species are released into the atmosphere. Hence, it is essential to develop novel catalytic technologies that can also function after the point of NO_x emission to the atmosphere.

In this regard, photocatalytic oxidative NO_x storage (PHONOS)^[12–18] presents an appealing alternative as it can store airborne NO_x in the solid state under ambient conditions after the point of NO_x discharge to the atmosphere. This approach requires the presence of only sunlight, water and oxygen (all of which are abundantly present in the atmosphere) and a photocatalytically active material.^[19] This methodology has been implemented in advanced construction materials to combat urban NO_x pollution, using mainly titanium dioxide (TiO₂) based

[a] E. Ebrahimi, Dr. M. Irfan, Dr. Y. Kocak, B. Karakurt, Prof. E. Ozensoy
Chemistry Department
Bilkent University
06800, Ankara (Turkey)
E-mail: ozensoy@fen.bilkent.edu.tr

[b] Dr. M. Irfan
Nanoscience and Catalysis Department
National Centre of Physics
44000, Islamabad (Pakistan)

[c] F. Shabani, Prof. H. V. Demir, Prof. E. Ozensoy
UNAM-National Nanotechnology Center
Bilkent University
06800, Ankara (Turkey)

[d] Dr. E. Erdem
SUNUM Nanotechnology Research Center
Sabanci University
34956, Istanbul (Turkey)

[e] Dr. E. Erdem
Faculty of Engineering and Natural Sciences
Sabanci University
34956, Istanbul (Turkey)

[f] Prof. H. V. Demir
Department of Electrical and Electronics Engineering and Department of Physics
Bilkent University
06800, Ankara (Turkey)

[g] Prof. H. V. Demir
School of Electrical and Electronic Engineering
School of Physical and Mathematical Sciences, and School of Materials Science and Engineering
Nanyang Technological University
639798, Singapore (Singapore)

 Supporting information for this article is available on the WWW under <https://doi.org/10.1002/cctc.202000749>

photocatalysts.^[20–22] TiO₂ is an abundant, cost-efficient, chemically and thermally stable semiconductor, which is extensively used in the photocatalytic decomposition of both gas and liquid-phase pollutants.^[23] Photocatalytic activity of TiO₂ is governed by a multitude of complex chemical, physical, optical and electronic properties, including (but not limited to) the phase/crystal structure, specific surface area (SSA), crystallite size and electronic band gap.^[24–26] Due to the relatively large band gap of TiO₂ (3.0–3.2 eV), it is commonly reported in the literature that TiO₂ enables the harvesting of mostly ultraviolet (UV-A) light, which constitutes only 4–5% of the solar spectrum.^[27] Therefore, development of visible (VIS) light-responsive photocatalysts with higher stability, selectivity and activity is highly desired. For this purpose, different strategies have been adopted to enhance the photocatalytic efficiency of TiO₂ in the VIS light region such as non-metal^[28–30] and precious/non-precious metal^[15,16,31–36] doping, functionalization with quantum dots (QDs)^[37–39] and surface modifications with polymers.^[40,41]

An important requirement in PHONOS applications is the high selectivity of the designed photocatalyst toward nitrate (NO₃[−]) formation, which is the preferred final storage product of the photocatalytic NO_x abatement process. In one of our recent reports,^[18] we have demonstrated the formation of nitrates on TiO₂ (P25) with different adsorption geometries (*e.g.* monodentate, bidentate and bridging nitrates) upon interaction of TiO₂ (P25) with NO₂ (g) *via in-situ* FTIR spectroscopy. Unfortunately, TiO₂ has an extremely low selectivity towards NO_x storage in solid state and tends to oxidize NO(g) into a more toxic product, NO₂ (g), which is ultimately released into the atmosphere.^[42] Therefore, it is necessary to develop TiO₂-based photocatalysts that can harvest light across a broad spectral window with high selectivity, efficiency and stability.

To achieve these challenging objectives, in the current work, two-dimensional (2D) rectangular CdSe (core)/CdSeTe (crown) quantum-well nanoplatelets (NPL) were synthesized and utilized in the modification of TiO₂ toward PHONOS applications. Semiconductor NPL (also known as colloidal quantum wells) provide novel opportunities in photocatalytic applications as their thicknesses, diameters, shapes, electronic and optical properties can be fine-tuned with high precision *via* colloidal synthesis and hetero-structure growth strategies.^[43,44] In addition, 2D semiconductor NPL can also be utilized to enhance light absorption/harvesting and photon-induced charge (electron and/or hole) transfer properties of the overall photocatalytic system. Quantum NPL systems can be more advantageous as compared to conventional quantum dot (QD) systems due to the stronger light absorbance capability of NPL, which can be attributed to the NPL's extraordinary large absorption cross-section per particle, associated with their very tight quantum confinement and the relatively larger volume.^[45,46] The faster charge transfer/charge separation capability of the NPL could originate from the extended surface area of the NPL and/or their continuous density of electronic acceptor states.^[47] Additionally, unlike conventional QDs, 2D quantum NPL have large linear and non-linear absorption cross sections and preferable excitonic features, rendering them

promising alternatives for zero-dimensional QDs.^[48] NPL heterostructures with different chemical compositions, vertical thicknesses and, architectures such as core-only,^[49] core/crown,^[50] core/shell,^[51] and core/crown/shell^[52] can be synthesized. Furthermore, particle size distribution and shape uniformity can also be controlled to achieve desired electronic structures and optical properties. Different band alignments between the core, crown, and shell materials may yield either Type-I or Type-II semiconductor heterojunctions,^[53] which can be fine-tuned for particular operational functionalities. In the current study, NPL systems (*i.e.* CdSe/CdSeTe) with Type-II heterojunctions are selected, since in these NPL, photo-excited electrons are expected to be localized in the CdSe core, while holes may be trapped in the CdSeTe crown, forming spatially indirect excitons with presumably much longer lifetimes (as compared to core/crown and core/shell NPL with a Type-I electronic structure, where both electron and hole wave functions are typically confined in the same region of the NPL).^[54–55] Apart from exhibiting strongly red-shifted emission along with significantly increased radiative fluorescence lifetimes, charge separation at the core/crown interface of Type-II heterostructures can also promote the suppression of non-radiative recombination/relaxation channels owing to their large in-plane exciton mobility.^[56] Our hypothesis here is that in the proposed CdSe/CdSeTe/TiO₂ composite system, photogenerated electrons from the CdSe/CdSeTe NPL can be injected to the conduction band of TiO₂, whereas the corresponding holes in the valence band of TiO₂ can be transferred to the valence band of CdSe/CdSeTe NPL.^[14,57,58] Such functionalization of TiO₂ with NPL is also expected to enhance the photon absorption in the VIS region of the solar spectrum. Hence, an improvement in the photocatalytic DeNO_x performance of TiO₂ is anticipated upon incorporation of NPL.

In the present study, CdSe/CdSeTe NPL were synthesized by using CdSe core as the seed. Then, core/alloyed crown of CdSe/CdSe_{0.75}Te_{0.25} was synthesized, where the crown layer was grown laterally while the vertical thickness was kept fixed. The structure of as-synthesized NPL was characterized and verified through a multitude of spectroscopic, diffraction and imaging techniques. Next, photocatalytic performance of NPL/TiO₂ composites were tested in NO photo-oxidation under environmentally relevant reaction conditions. A noteworthy enhancement in the photocatalytic activity and selectivity of TiO₂ (P25) was observed upon functionalization with NPL.

Results and Discussion

Structural analysis by XRD

Crystal structures of CdSe/CdSeTe NPL, P25 (TiO₂), as well as CdSe/CdSeTe/P25 with different NPL loadings were investigated *via* XRD. The peaks at 2θ values of 24.69°, 29.02°, 41.23° and 48.85° were attributed to (111), (200), (220) and (311) facets of the CdSe core of NPL; respectively (Figure 1a). As mentioned in the former reports,^[55] addition of a CdSeTe crown to the CdSe core did not lead to major changes in the XRD pattern of the

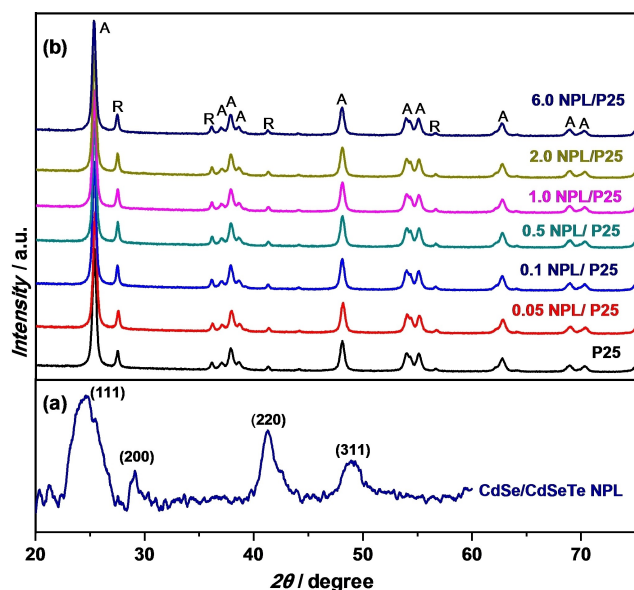


Figure 1. XRD patterns of (a) CdSe/CdSeTe NPL (without TiO_2), and (b) pure P25, and CdSe/CdSeTe/P25 composite materials with various NPL loadings. A: anatase, R: rutile.

CdSe core. XRD profile of P25 in Figure 1b demonstrates characteristic diffraction signals of TiO_2 , confirming the presence of anatase (ICDD card no. 00-021-1272) and rutile (ICDD card no. 00-021-1276) domains. Diffraction patterns of the CdSe/CdSeTe NPL/P25 composites are similar to that of P25 due to the miniscule loadings of NPL used in the functionalization of P25 and the small NPL particle sizes. Currently used minute loadings of CdSe/CdSeTe NPL were chosen in order to minimize material cost and toxicity.

Electron microscopy analysis via TEM

Several representative TEM images of the CdSe/CdSeTe core/crown NPL (in the absence of TiO_2) are shown in Figure 2. Synthesized NPL exhibited rectangular and uniform shapes with dimensions of ca. $90 \text{ nm} \times 30 \text{ nm}$. The stacks of NPL in these images clearly reveal the uniformity of these quasi-2D nanostructures both in terms of lateral dimensions as well as thickness.

Surface structural analysis via XPS

In order to examine the surface chemistry, electronic structure and elemental composition of the core/crown NPL, XPS measurements (Figure 3) were carried out (additional data and discussion about the XPS results are provided in the SI section, Figures S1 and S2). In the XPS measurements, fresh CdSe/CdSeTe NPL in the absence of TiO_2 (Figures 3a–3e), CdSe/CdSeTe/ TiO_2 (NPL/P25) composite system before and after 5 h PHONOS reaction under UV-A (Figure 3f) or VIS irradiation (Figure 3g) were investigated.

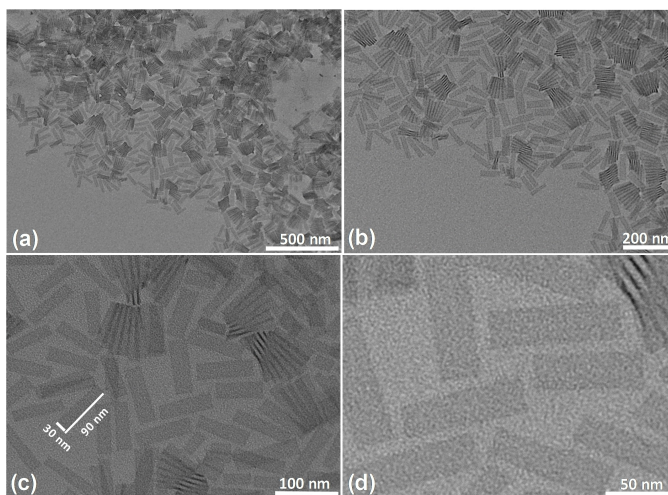


Figure 2. (a–d) Representative TEM images of CdSe/CdSeTe NPL with different magnifications.

$\text{O}1s$ spectrum of the fresh NPL without TiO_2 revealed a broad and a convoluted signal (Figure 3a) associated with the C–O, C=O and O–H functionalities of the oleic acid capping of the NPL (see experimental section for the synthesis details of NPL).^[59] Figure 3b presents the corresponding $\text{C}1s$ spectrum of fresh NPL without TiO_2 , where the shoulder visible at 288.1 eV can be ascribed to C–O and C=O functionalities of the oleic acid capping and the larger signal at 284.8 eV can be attributed to C–C linkages of oleic acid as well as the surface (adventitious) carbon species. Note that binding energy (B. E.) positions of the spectra in Figures 3a–3e for the fresh NPL without TiO_2 were calibrated using the adventitious carbon signal at 284.8 eV while the spectra in Figures 3f–3g were calibrated using the Ti^{4+} features of P25 (TiO_2) (i.e. $\text{Ti}2p_{3/2}$ and $\text{Ti}2p_{1/2}$ features at 458.5 eV and 464.1 eV, respectively^[14,60]). Figures S1 and S2 show that in the case of NPL/P25 composite system, $\text{O}1s$ and $\text{C}1s$ signal intensities diminish after PHONOS reaction under UV-A or VIS illumination due to decomposition of the oleic acid capping functionalities and possibly photo-desorption of $\text{CO}_x/\text{H}_x\text{C}_y\text{O}_z$ species. This is also in line with the growth of the $\text{Ti}2p$ signal intensities (Figures S1 and S2) after PHONOS reaction on NPL/P25 composite system under UV-A or VIS illumination indicating increasing exposure of TiO_2 to incoming X-rays after the decomposition of the oleic acid capping of the NPL. XPS data for the Cd, Te and Se regions (Figures 3c–3e), reveal close resemblance to the multicomponent quantum dot systems, containing heterojunctions including both CdSe and CdTe domains.^[61–63] Hence, $\text{Cd}3d_{5/2}$ feature at 405.1 eV in Figure 3c is consistent with the Cd species interacting with Te and/or Se species^[61–63] and lack of significant amounts of CdO_x species. The $\text{Te}3d_{5/2}$ feature located at 572.5 eV in Figure 3d can be assigned to Te species that are interacting with Se and/or Cd.^[60–64] Likewise, the broad and complex $\text{Se}3d$ signal in Figure 3e shows a $\text{Se}3d_{5/2}$ B. E. of ca. 53.9 eV in accordance with the existence of CdSe and CdSeTe species. Thus, XPS results given in Figure 3 are in line with the presence of closely

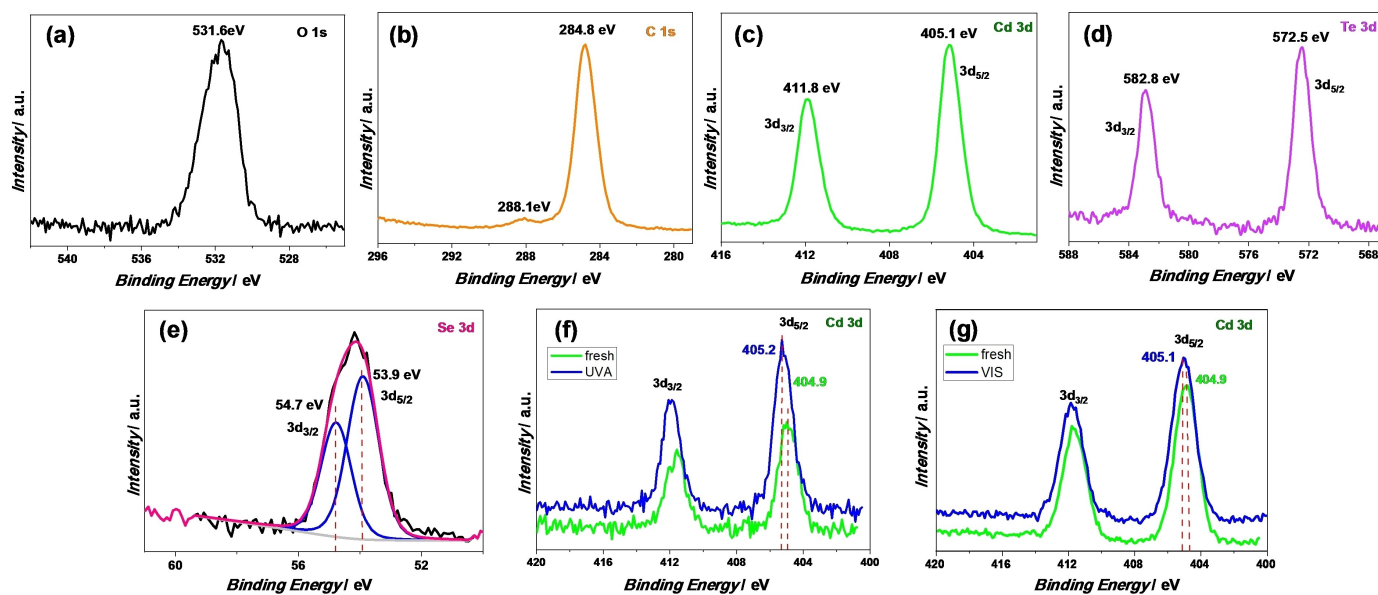


Figure 3. XPS spectra of fresh (as prepared) CdSe/CdSeTe NPL (in the absence of TiO₂): (a) O1s, (b) C1s, (c) Cd3d, (d) Te3d, and (e) Se3d regions. Cd3d XPS spectra for CdSe/CdSeTe/TiO₂(P25) composites before (green) and after (blue) 5 h PHONOS reaction under (f) UV-A, and (g) VIS illumination.

interacting Cd, Se and Te species as would be expected in the CdSe/CdSeTe NPL. Post-reaction XPS analysis of the CdSe/CdSeTe/TiO₂(P25) composites indicate blueshifts in the Cd3d_{5/2} B. E. after PHONOS reaction under UV-A or VIS illumination suggesting that detectable electronic structural changes occur in the CdSe/CdSeTe/TiO₂ composite system upon extensive UV-A or VIS aging under PHONOS reaction conditions, resulting in partial oxidation of Cd sites (apparent by the blue shift in Cd3d B.E.). Presumably, these electronic structural changes could be due to the photo-oxidation of Cd species, as well as due to the changes in the chemical environment of Cd and Te surface species upon partial photo-degradation of the oleic acid capping agent. Note that electronic structural alterations of the Te and Se sites of the CdSe/CdSeTe/TiO₂ system could not be accurately analyzed via XPS due to the Ti2s loss feature of TiO₂ overwhelming Te3d region and the small XP cross-section of Se falling below the detection limit.

Specific surface area (SSA) analysis with BET

SSA of pure P25 was found to be 50 m²/g, while SSA of 0.05NPL/P25, 0.1NPL/P25, 0.5NPL/P25, 1.0NPL/P25 and 2.0NPL/P25 were determined to be 44, 45, 41, 40 and 39 m²/g, respectively. This minor decrease in SSA with increasing NPL loading can be attributed to the partial blocking of the P25 pores by NPL.

Electronic structural analysis via UV-VIS and photoluminescence spectroscopy

Absorption and PL spectra of 4 ML CdSe/CdSeTe NPL (in the absence of TiO₂) is presented in Figure 4a. Absorption spectrum in Figure 4a reveals light-hole (lh) and heavy-hole (hh) transition of the CdSe core of CdSe/CdSeTe NPL at 482 and 512 nm, respectively.^[65] It was demonstrated in one of our former reports that,^[65] these sharp excitonic transitions in the absorption spectrum of core-only CdSe remain almost intact during the lateral growth of CdSeTe crown, irrespective of CdSeTe crown size. When CdSeTe-crown layers are laterally grown on CdSe core seed, a new absorption peak at 563 nm is observed for CdSe/CdSeTe NPL due to the light-hole electron transition in the CdSeTe crown.^[65] It is apparent from Figure 4a that both CdSe core and CdSeTe crown regions contribute to the absorption spectrum in agreement with the formation of CdSe/CdSeTe core/crown NPL having Type-II band alignment. PL spectrum in Figure 4a also presents an emission peak at 591 nm with a full width at half maximum (FWHM) of 45 nm. PL spectra of P25 and CdSe/CdSeTe NPL given in Figure S3 also show that the presence of NPL suppresses the photoluminescence of P25 (titania) which is consistent with the enhanced electron-hole separation and extended exciton lifetime. Figure 4b presents the Tauc plot for the CdSe/CdSeTe NPL (without P25) revealing a direct band gap of 2.45 eV for the CdSe core and 2.14 eV for the CdSeTe crown. These values further support the formation of a VIS-light-driven Type II heterojunction in CdSe/CdSeTe NPL, where the outer crown/shell (which can also include Te-doped CdSe domains) can have a stronger VIS-light absorption as compared to the inner core material.^[66]

Since the conduction band edge of CdSe core lies lower in energy than that of CdSeTe crown,^[65] during the photoexcita-

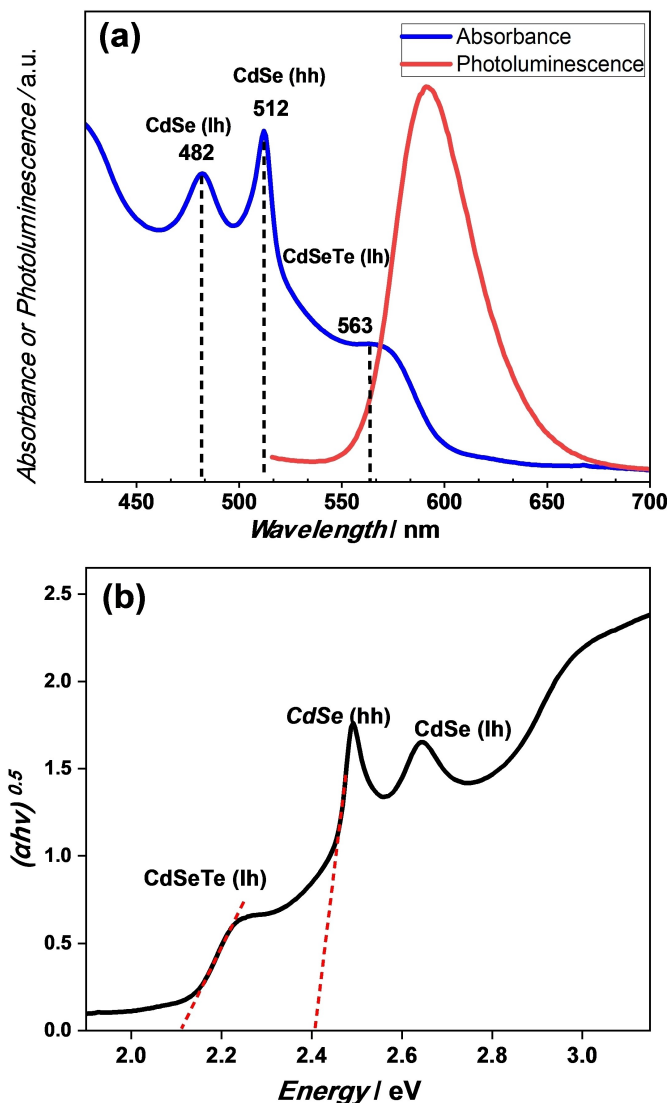


Figure 4. (a) Absorbance and photoluminescence spectra of 4 ML-thick bare CdSe/CdSeTe NPL (*i.e.* without TiO₂) dispersed in toluene; (b) Tauc plot for bare CdSe/CdSeTe NPL.

tion of the CdSe/CdSeTe/P25 system, excited photoelectrons in the conduction band of the CdSeTe crown can be transferred to the conduction band of the CdSe core which can ultimately be transported to the conduction band of the TiO₂ (Figure 5). In turn, generated holes can be confined in the CdSeTe crown valence band.^[67]

Equations (1–2)^[68–69] and the band gap energies (determined from Figure 4) of various structural components in the NPL and NPL/TiO₂ system (*e.g.* CdSe, CdSeTe, and TiO₂) can be used to estimate the valence band and conduction band positions of these components:

$$E_c^0 = E_e - X_{AB} + 0.5 E_g \quad (1)$$

$$X_{AxBy} = (X_A^x \cdot X_B^y)^{1/(x+y)} \quad (2)$$

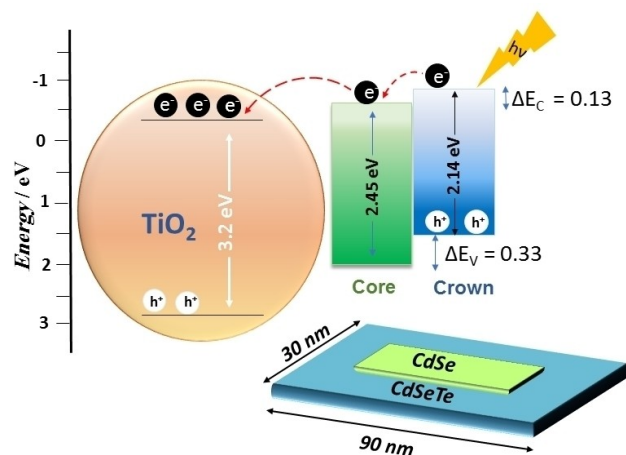


Figure 5. Electron energy diagram for core/crown CdSe/CdSeTe NPL on TiO₂.

Here E_c is the conduction band potential, X_{AB} is the electronegativity of the semiconductor expressed as the geometric mean of the absolute electronegativity of the constituent atoms, x and y are stoichiometric coefficients in the empirical formula, E_e is the energy of free electrons on the hydrogen scale (*i.e.* 4.5 eV)^[69] and E_g is the bandgap. Electron energy diagram for the CdSe/CdSeTe/TiO₂ system, based on the estimated energy positions are summarized in Figure 5. Electron transfer cascade shown in Figure 5 may yield efficient electron-hole separation, extended exciton lifetime and suppression of the electron-hole recombination processes, which we believe are associated to the origins of the photocatalytic activity boost of the CdSe/CdSeTe/TiO₂ composite system studied in the current work.

Electron and hole trapping analysis of CdSe/CdSeTe NPL via EPR spectroscopy

In an attempt to understand the influence of UV irradiation on the electronic structure of the CdSe/CdSeTe NPL, we performed *in-situ* EPR experiments under dark as well as under 2 h-long UV irradiation (Figure 6). In the former *in-situ* EPR studies, trapping of electrons in the colloidal InP system upon optical excitation was reported.^[70] Since the typical life times of such electron trapping events are rather short (in the order of 10⁻⁹–10⁻³ s^[71,72]), long-life time (10¹–10² s) radical spin traps such as 2,2,6,6-tetramethylpiperidin-1-yl) oxidanyl (TEMPO) or 5,5-dimethyl-pyrroline N-oxide (DMPO) or metal cation dopants such as Mn²⁺ were externally added to the analyzed samples to allow longer data acquisition times with a higher signal to noise ratio (S/N).^[73–75] In the current *in-situ* X-band EPR measurements, no external spin-trap agents were added to the measured samples. Figure 6 reveals no detectable EPR signals for CdSe/CdSeTe NPL in dark. However, UV irradiation leads to the emergence of a new EPR signal (Figure 6) suggesting the generation of paramagnetic states in NPL. Due to the corresponding *g*-factor of the detected EPR signal, it is likely

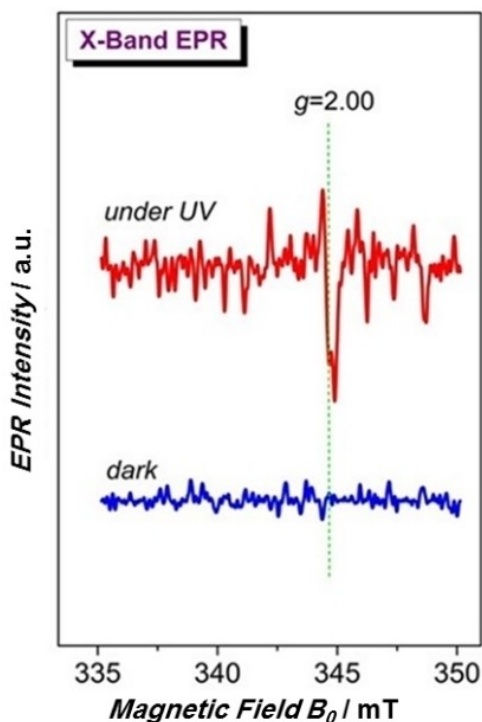


Figure 6. Room temperature X-band EPR spectra of CdSe/CdSeTe NPL (without TiO₂) under dark and UV illumination conditions.

that this is new signal which is occurring only in the presence of UV irradiation is due to photo-induced electron transfer from the CdSeTe crown to the CdSe core of the quantum well system, where electron-trapping occurs in the CdSe core. While trapped electrons and trapped holes yield similar g -values (g_e

$= 2.0023^{[76]}$) in EPR, detection of trapped hole states in EPR is difficult due to the significantly smaller EPR intensities of hole states.^[77] It should be noted that control EPR experiments performed on P25 under UV irradiation and under dark conditions did not yield any evidence for such charge carriers, suggesting that most of the photo-induced charge carriers originated from NPL (Figure S4). Thus, current EPR data supports the synergistic electronic effect of the CdSe/CdSeTe NPL in the CdSe/CdSeTe/TiO₂ composite system extending the electron-hole recombination lifetime which presumably has a positive influence on the photocatalytic activity, as will be described in the further sections. Note that EPR signals for the experiments performed on CdSe/CdSeTe/TiO₂ were below the detection limit, due to the small concentration of NPL present in the NPL/P25 system and thus not shown here.

Photocatalytic NO_x(g) oxidation and storage (PHONOS) performance tests

Figure 7a pictorially summarizes the PHONOS process while, Figure 7b shows the typical time-dependent NO(g), NO₂(g) and total NO_x(g) (*i.e.* NO(g)+NO₂(g)) concentration profiles as a function of the VIS-light irradiation time during the NO photo-oxidation over 0.1NPL/P25 photocatalyst. In the first stage of the photocatalytic activity tests, a synthetic polluted air gas mixture containing *ca.* 1 ppm NO(g) was fed to the photocatalyst surface under dark conditions. During this initial phase (*i.e.* 0–5 min), a minor transitory fall in the total NO_x(g) and NO(g) concentrations was observed due to adsorption of NO_x species on the reactor lines, expansion of the gas in the reactor as well as non-photocatalytic adsorption of NO_x on the photocatalyst surface. In addition, a tiny amount of NO₂(g) was

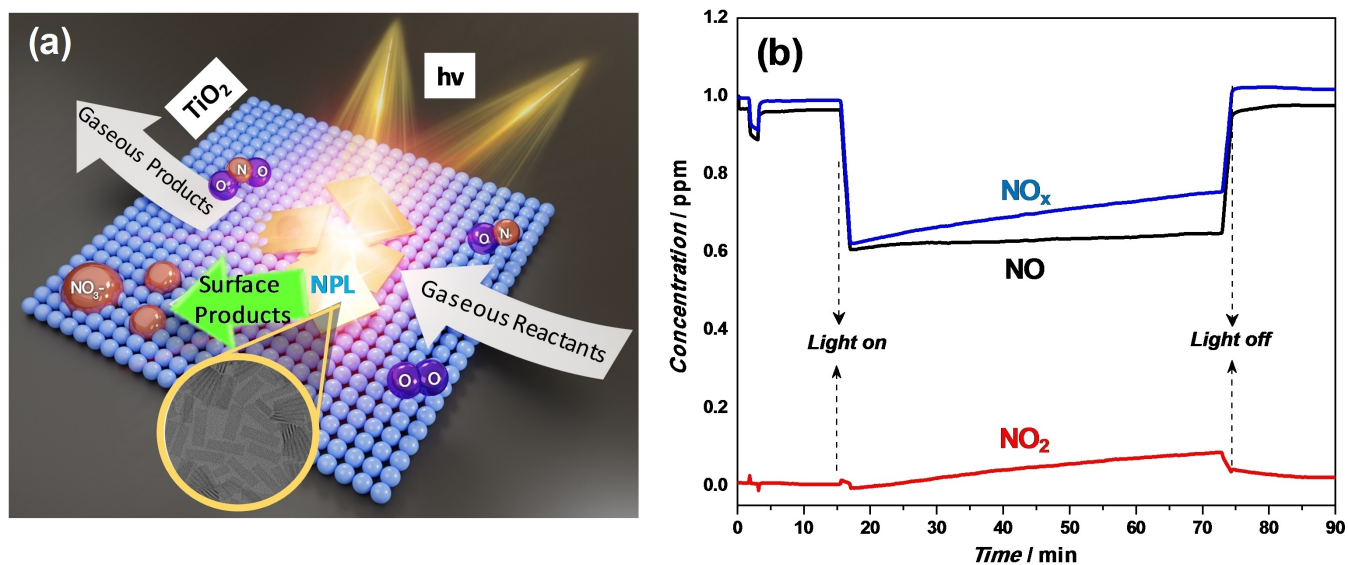


Figure 7. (a) Schematic representation of PHONOS process. (b) Concentration vs. time profiles for a typical PHONOS activity test performed with 0.1NPL/P25 under VIS irradiation. Red (bottom), black (middle) and blue (top) traces correspond to NO₂(g), NO(g) and total NO_x (*i.e.* NO(g)+NO₂(g)) concentrations, respectively. Feed composition: N₂(g) 0.750 SLM, O₂(g) 0.250 SLM, and NO(g) 0.010 SLM (100 ppm NO(g) diluted in balance N₂(g), 50% relative humidity (RH) at 23 °C.

produced due to thermal catalytic processes occurring on the catalyst surface. Following the saturation of the reactor system and photocatalyst surface, $\text{NO}_x(\text{g})$ and $\text{NO}(\text{g})$ levels quickly returned to the original inlet values and reached a steady state in dark conditions.

Next, UV-A or VIS-light irradiation was turned on after the first ca. 15 min (Figure 7b) and a drastic fall in the $\text{NO}(\text{g})$ and total $\text{NO}_x(\text{g})$ concentrations was detected along with a small increase in the $\text{NO}_2(\text{g})$ level. While the latter observation clearly shows the photocatalytic oxidation of $\text{NO}(\text{g})$ into $\text{NO}_2(\text{g})$, decrease in the $\text{NO}(\text{g})$ and total $\text{NO}_x(\text{g})$ concentrations indicates that in addition to this process, solid state storage of $\text{NO}(\text{g})$ and $\text{NO}_2(\text{g})$ in the form of chemisorbed NO_2 , nitrites and/or nitrates also occur on the photocatalyst surface.^[6,78,79] In principle, $\text{N}_2(\text{g})$ and/or $\text{N}_2\text{O}(\text{g})$ can also be produced as a result of direct photocatalytic decomposition and photo-reduction of $\text{NO}(\text{g})$.^[80] However, this is known to be a relatively inefficient reaction pathway, particularly in the presence of O_2 and H_2O . Thus, N_2 and/or N_2O formation can readily be ruled out in the current study.^[17] It is apparent in Figure 7b that photocatalytic NO_x abatement action continues after this initial stage during the entire duration of the activity test. Thus, total NO_x abatement effect can be calculated by integrating the relevant concentration traces for the entire duration of the PHONOS test.

Photocatalytic performance of fresh and aged CdSe/CdSeTe/P25 catalysts under UV-A light

PHONOS activity tests were performed for the fresh and aged NPL/P25 photocatalysts with different loadings and compared with that of a commercial benchmark P25 (titania) photocatalyst under identical experimental conditions. Details of the photocatalytic performance parameters and Figures of merits used for performance comparison are described in detail in the Supporting Information section along with the supplementary photonic efficiency data (Figures S5–S8). Aged catalysts used in the UV-A PHONOS performance tests were prepared by exposing the NPL/P25 catalysts to an UV-A light source for 18 h

under ambient conditions prior to the photocatalytic activity measurements. It is apparent from Figure 8 and Figure S5 that P25 reveals a rather high NO conversion % (33%) while yielding a very low NO_x storage selectivity % (23%) due to the production of large quantities of unwanted $\text{NO}_2(\text{g})$. Although TiO_2 has a much higher adsorption capacity for $\text{NO}_2(\text{g})$ than that for $\text{NO}(\text{g})$,^[81] photocatalytic $\text{NO}_2(\text{g})$ production rate and the total amount of NO_2 generated readily overwhelms the NO_x adsorption capacity of titania leading to unwanted $\text{NO}_2(\text{g})$ release into the atmosphere. As $\text{NO}_2(\text{g})$ is a much more toxic pollutant than $\text{NO}(\text{g})$, P25 does not qualify as an efficient photocatalyst for NO_x abatement under UV-A light irradiation, evident by the extremely negative DeNO_x index values of fresh (−0.42) and aged (−0.45) P25 given in Figure 8. Incorporation of different loadings of CdSe/CdSeTe NPL to P25 results in enhanced PHONOS performance under UV-A irradiation (Figure 8a). For the fresh 0.05 NPL/P25 photocatalyst, NO conversion % and NO_x storage selectivity % values reach 41% and 81% under UV-A illumination, respectively (Figure 8a). For the fresh NPL/P25 photocatalysts increasing NPL loadings within 0.1–2.0 mL monotonically enhance the PHONOS performance, where NO conversion % and NO_x storage selectivity % values of 44% and 94% can be achieved for 2.0NPL/P25 sample, respectively. In contrast, a further increase in NPL loading (*i.e.* for 6.0NPL/P25) results in a deteriorated performance. We believe that the attenuation of PHONOS performance at high NPL loadings is due to the blocking of the photocatalytic active sites of titania or substitution of the surface –OH functionalities of titania with oleic acid capped-NPL.

It is apparent that fresh 2.0NPL/P25 photocatalyst is capable of storing significant amounts of NO_x in the solid state and suppresses $\text{NO}_2(\text{g})$ release significantly under UV-A irradiation. These results clearly demonstrate that proper incorporation of NPL to titania (P25) alters the unfavorably negative DeNO_x index of P25 (−0.42) to a significantly positive value (+0.35) under UV-A illumination (Figure 8b). The mechanism for the photocatalytic oxidation of NO on TiO_2 has been studied in detail in former reports and the previously proposed mechanisms consist of multiple pathways which yield nitrites and/or

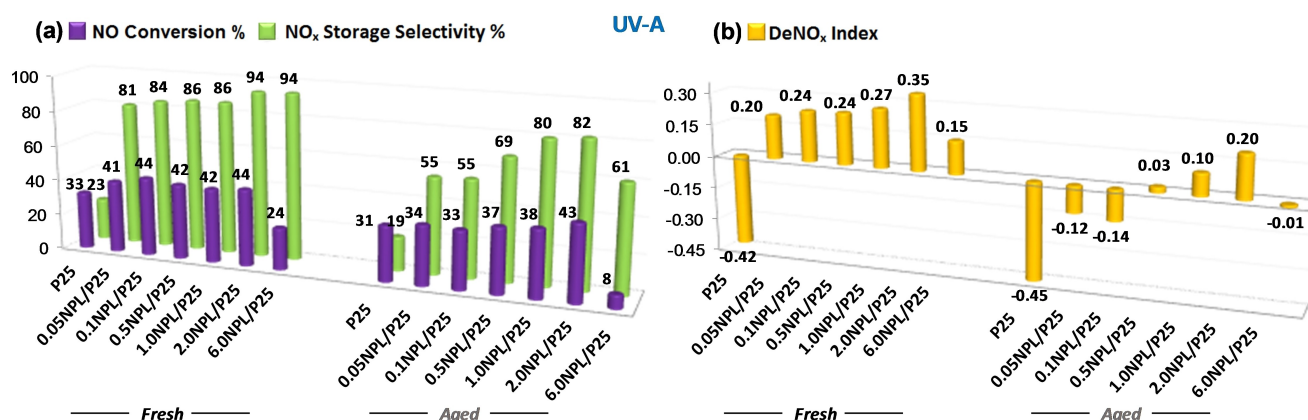
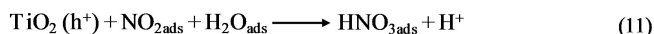
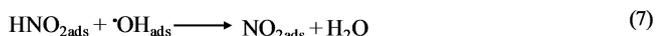
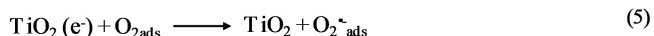
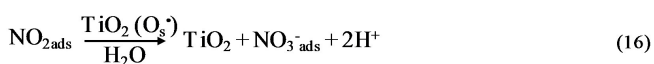
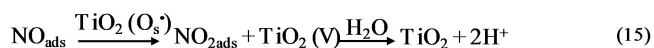
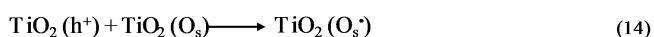
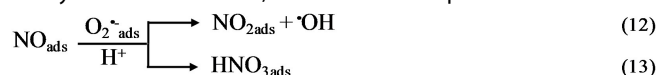


Figure 8. $\text{NO}(\text{g})$ conversion %, NO_x storage selectivity % and DeNO_x index values for different NPL/P25 composite photocatalysts obtained under UV-A irradiation.

nitrites (along with their protonated acidic forms) as the primary products.^[82–85] Formation of nitrites in similar processes was also demonstrated *via in-situ* FTIR spectroscopy in one of our former reports.^[18] NO photooxidation on TiO₂ starts with the absorption of photons by TiO₂ which leads to the generation of electron and hole (*i.e.* e⁻-h⁺) charge carriers and proceeds with the trapping of these charge carriers to form various surface species (eq. 3–5). Next, adsorbed NO on the TiO₂ surface is photo-oxidized *via* its interaction with surface hydroxyl radicals ([•]OH_{ads}) or holes (h⁺) to form NO₂. Alternatively, hydroxyl radicals (eq. 6–8) or holes (eq. 9–11) can also attack adsorbed NO₂ species to form HNO₃.



Ohko *et al.*^[85,86] proposed an alternative photocatalytic NO oxidation mechanism on TiO₂ involving lattice oxygen species. In this mechanism, NO oxidation can be carried out either *via* superoxide radical anions (eq. 12–13) or *via* an electron deficient surface oxygen species (eq. 14–16). Furthermore, adsorbed water can also play an important role in the photocatalytic oxidation of NO, as indicated in eq. 3–16.^[82]



Aging of the NPL/P25 photocatalysts under UV-A irradiation for 18 h under ambient conditions leads to interesting variations in the photocatalytic performance trends (Figure 8). For the NPL loadings within 0.05–2.0 mL, although, NO conversion is not significantly affected by UV-A aging, selectivity severely decreases (Figure 8a). Nevertheless, despite the loss in PHONOS performance, some of these aged photocatalysts are able to yield significantly positive DeNO_x index values. This decrease in the photocatalytic performance of the NPL/P25 system upon UV-A aging can be ascribed to the degradation/decomposition of the oleic acid capping of the NPL^[87] and/or electronic changes in the CdSe and CdSeTe domains (such as oxidation of Cd sites), as suggested by the current XPS data (Figure 3). It is interesting to note that NO conversion capability of the NPL/P25 system is only slightly affected by the aging process (Figure 8), suggesting that a majority of the photocatalytic NO oxidation active sites on titania remained intact

and could still function efficiently even after aging under UV-A. On the other hand, aging of 6.0NPL/P25 system with the highest NPL loading leads to a drastic loss in both NO conversion activity as well as in NO_x storage selectivity (Figure 8a). This is probably due to the extended obstruction of the photocatalytic active sites and NO_x storage sites of titania and CdSe/CdSeTe domains of the 6.0NPL/P25 system with the abundant oleic acid degradation products; evident by the very low DeNO_x index of aged 6.0NPL/P25 (−0.01), as shown in Figure 8b.

Photocatalytic performance of fresh and aged catalysts under VIS light

Figure 9a indicates that fresh P25 titania photocatalyst has a reasonably good NO conversion and NO_x storage selectivity under VIS irradiation (as in the case of UV-A irradiation). It is interesting to note that even though P25 titania is commonly considered to be an UV-active photocatalyst, current results demonstrate that it also reveals significant PHONOS activity under VIS illumination. Commercially available P25 titania used in our measurements typically contains 78–85 wt.% anatase, 14–17 wt.% rutile and 0–13 wt.% amorphous titania phases constituting a variety of heterojunctions which can also reveal significant photocatalytic NO conversion under VIS-light. In addition, currently used photon flux values utilized in the VIS experiments were greater than that of the UV-A experiments (see section 2.4). Hence, photonic efficiency % results presented in Figure S6, suggest significantly lower NO_x storage photonic efficiency % for P25 under VIS illumination compared to that of UV-A (due to the normalization of conversion values with photon flux in the photonic efficiency % definition), despite the fact that both illumination sources reveal rather comparable NO conversion % and NO_x storage Selectivity % values (Figures 8 and 9). It is important to note that as in the UV-A case, VIS-aging does not lead to significant detrimental changes in the PHONOS performance of P25. Furthermore, fresh and aged P25 samples lead to significantly negative and unfavorable DeNO_x index values under VIS-light illumination (Figure 9b), suggesting that without NPL, P25 cannot store photogenerated NO₂ effectively and instead, releases toxic NO₂(g) into the atmosphere. Incorporation of NPL to P25 titania resulted in a minor increase in NO conversion % along with a drastic boost in NO_x storage selectivity % under VIS irradiation (Figure 9a). For the fresh NPL/P25 photocatalysts with different NPL loadings, a volcano plot in performance is visible, both in terms of NO conversion %, NO_x storage selectivity % (Figure 9a), as well as in terms of DeNO_x index values (Figure 9b). It is seen that fresh 0.1NPL/P25 provided the best NO conversion % along with the most positive DeNO_x index value (+0.30) under VIS illumination. The best PHONOS performance under VIS irradiation was achieved with a comparatively lower loading of NPL on P25 (0.1NPL/P25) as compared to the UV-A case, where in the latter case the best performance was observed for the 2.0NPL/P25 sample. This important difference highlights the dissimilarities in the corresponding photocatalytic reaction mechanisms

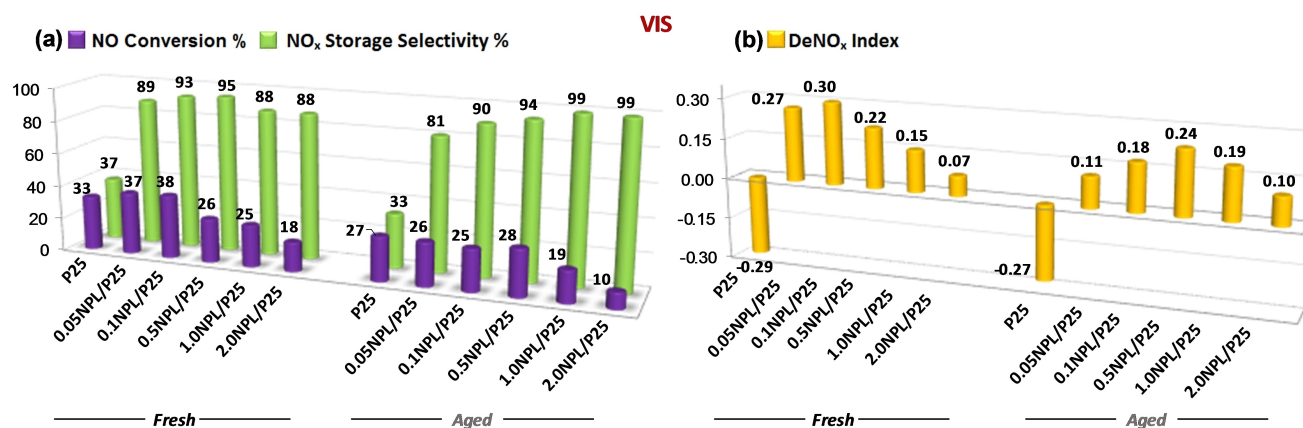


Figure 9. NO(g) conversion %, NO_x storage selectivity %, and DeNO_x index values for different NPL/P25 photocatalysts obtained under VIS-light irradiation.

driving the PHONOS process under UV-A vs. VIS illumination. Some of these important differences in the photocatalytic reaction mechanisms as well as variations in the nature and coverage of various surface species/intermediates formed during the PHONOS reaction under UV-A vs. VIS will be elucidated in our forthcoming reports utilizing a dedicated photocatalytic flow reactor equipped with *in-situ* vibrational spectroscopic capabilities. As discussed in the previous section, current results suggest that the primary photocatalytic site for NO oxidation on the NPL/P25 system resides on titania, while a synergistic effect between titania and NPL results in an additional increase in NO conversion capability. On the other hand, the major function of oleic acid-capped NPL is the photocatalytic conversion and storage of photogenerated NO₂ species into other oxidized surface species, such as HONO, HONO₂, NO₂⁻ and NO₃⁻. It is apparent that for extremely high loadings of NPL on P25, PHONOS performance gradually decreases due to the blocking of the titania active sites with NPL. Aging of the NPL/P25 photocatalysts under VIS irradiation for 18 h decreases the NO conversion % and thus leads to lower rates of NO₂(g) generation enabling a more efficient NO_x capture by the photocatalyst resulting in a higher NO_x storage selectivity %. It is important to mention here that VIS-aging has a comparatively less drastic effect on the overall performance of NPL/P25 (Figure 9) as compared to that of UV-A-aging (Figure 8), probably due to the higher stability of NPL and oleic acid capping agent under VIS irradiation as demonstrated by the current C1s XPS data given in Figure S2. Additional aging experiments (data not shown) carried out on the 0.1NPL/P25 photocatalyst under UV irradiation for 18 h followed by PHONOS tests under VIS illumination showed that this catalyst was able to maintain 79% of its original NO conversion capability, 90% of its original NO_x storage selectivity under VIS irradiation after UV aging.

Thus, the best overall PHONOS performance among VIS-aged samples in terms of DeNO_x index is achieved for the 0.5NPL/P25 catalyst (Figure 9b). Hence, in order to circumvent VIS-aging effects, increasing NPL loading from 0.1 to 0.5 could be an efficient approach that can extend the catalytic lifetime

of NPL/P25 photocatalytic architecture with a minor sacrifice in the performance of the fresh NPL/P25 catalytic system.

Effect of NPL dispersing medium (toluene) on the photocatalytic performance

In the current work, before the incorporation of P25 with NPL, NPL were initially dispersed in toluene (C₆H₅CH₃ (l)) and then transferred onto the P25 surface (see experimental section). Hence, it is important to know whether toluene adsorption on P25 influences PHONOS performance. In an attempt to address this issue, additional control experiments were performed by dosing various amounts of C₆H₅CH₃ (l) on P25 at room temperature followed by evaporation and drying at 70 °C for 18 h.

Various amounts of C₆H₅CH₃ (l) on P25 at room temperature followed by evaporation and drying at 70 °C for 18 h. Along these lines, fresh and UV-A or VIS-aged T/P25 samples were prepared using the same volumes chosen for the preparation of the NPL/P25 composite systems. Then, PHONOS performances of these samples were tested under UV-A (Figures 10a and 10b) or VIS illumination (Figures 10c and 10d). It is interesting to observe that addition of increasing loadings of toluene leads to an increase in NO conversion % and NO_x storage selectivity % of fresh P25 under both UV-A and VIS light. While the enhancement in the PHONOS performance of fresh P25 due to toluene dosing cannot account for the entire photocatalytic enhancement observed for the NPL/P25 system, it clearly reveals some contribution to the observed performance boost. It is likely that in the presence of UV-A or VIS illumination, fresh P25 surface can carry out partial oxidation (as well as total oxidation) of toluene, resulting in the formation of various surface species (such as aromatic oxygenates with –OH, –COH, –COOH, functionalities etc.),^[88] which may expedite the NO and NO₂ adsorption. Thus, facilitated adsorption and increased surface residence times of NO (ads) and NO₂ (ads) species on the P25 surface, may enhance the oxidative storage of such species and improve PHONOS performance. On the other hand, extensive (18h) irradiation of the T/P25 samples with UV-A or

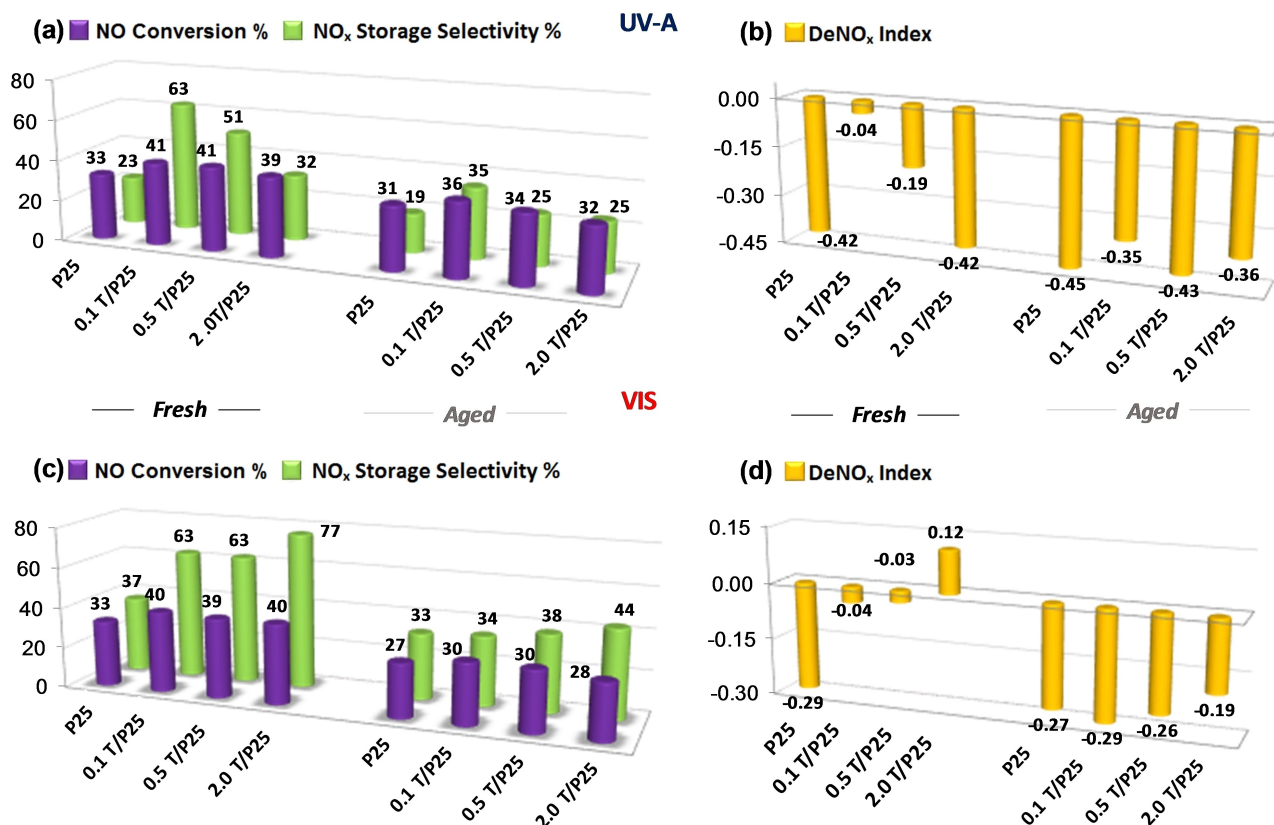


Figure 10. NO(g) conversion %, NO_x storage selectivity % results and the corresponding DeNO_x index values obtained under UV-A (a, b), and VIS illumination (c, d) for P25 photocatalysts dosed with various amounts of toluene (C₆H₅CH₃ (l)).

VIS light seems to eliminate the favorable influence of toluene on P25 PHONOS performance due to total oxidation of toluene and its partial oxidation products to CO₂(ads,g) and H₂O(ads,g). Hence, it is likely that while toluene may have a small but measurable positive influence on the PHONOS performance of the fresh NPL/P25 samples investigated in Figures 8 and 9, its effect on the (18 h UV-A or VIS) aged samples seems to be rather insignificant.

Photochemical stability of NPL/P25 composites and reusability

To demonstrate the photocatalytic reusability of the NPL/P25 materials, a series of experiments were performed on the best performing catalyst for each illumination type, where five successive 1 h-long PHONOS tests were carried out under UV-A or VIS-light on 2.0NPL/P25 or 0.1NPLs/P25, respectively (Figure 11). Under UV-A illumination, initial NO conversion % of 2.0 NPLs/P25 remained invariant, while its initially high NO_x storage selectivity % (*i.e.* 93%) monotonically decreased to 47% after five runs (Figure 11a). In addition, under UV-A irradiation, DeNO_x index values of 2.0NPL/P25 also rapidly declined and became negative after the second cycle (Figure 11b). This monotonic attenuation in NO_x abatement capability could be probably due to the continuous accumulation of nitrites/nitrates on the

photocatalyst surface diminishing the NO_x storage capacity and facilitation of NO₂(g) desorption/release via nitrate reduction. It is important to note here that identical stability experiments performed with titania P25 benchmark catalyst (data not shown) also revealed a monotonically decreasing DeNO_x index values where the values ranged between -0.32 and -0.37. Similarly, under VIS illumination, NO conversion of 0.1NPL/P25 remained relatively constant after five runs, while initial NO_x storage selectivity % (93%) decreased slightly (to 78%), maintaining a positive DeNO_x index value after five runs (Figures 11c and 11d).

Effect of temperature on photocatalytic performance during VIS irradiation

During the UV-A activated PHONOS tests, temperature of the photocatalytic reactor stayed within 20–25 °C, while it reached up to 46 °C during the VIS-light experiments. This is due to the differences in the emission spectra of the UV-A vs. VIS light sources employed in these tests. Therefore, it is important to understand the contribution of the temperature and validate that the observed catalytic enhancement under VIS light illumination originates from photocatalytic processes and not due to thermal catalytic routes. In order to address this issue, temperature of the photocatalytic reactor was varied by

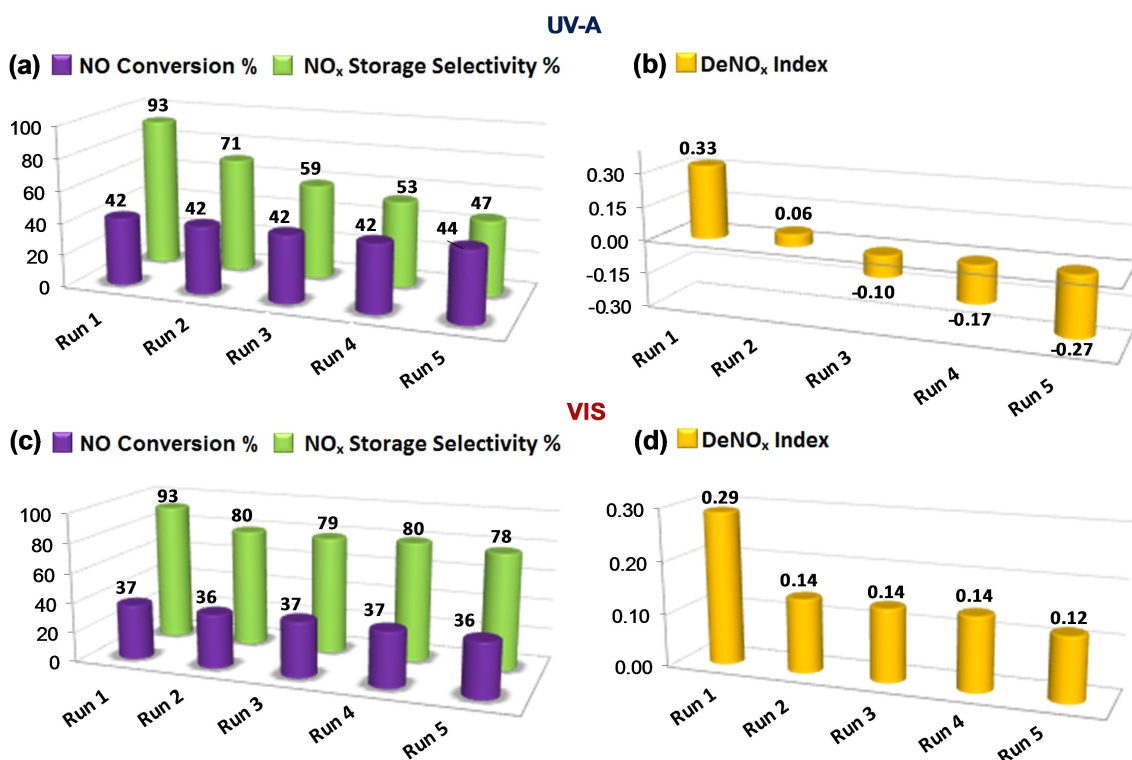


Figure 11. Long-term NO conversion % and NO_x storage selectivity % results and the corresponding DeNO_x index values obtained for five consecutive 1 h-long PHONOS tests under UV-A (a, b), and VIS illumination (c, d). UV-A experiments were performed with 2.0NPL/P25, while VIS experiments were performed with 0.1NPL/P25.

changing the distance between the VIS-light source and the reactor. VIS photon flux was decreased by increasing the distance between the VIS-light source and the reactor, which ultimately led to lowering of the reactor temperature during PHONOS tests. Next, photocatalytic performance of fresh P25 and 0.1NPL/P25 samples were measured under VIS-light illumination at different reactor temperatures, as shown in Figure 12. It should be emphasized that since absolute NO

conversion % and NO_x storage selectivity % values directly depend on the utilized VIS photon flux, these values cannot be used to compare PHONOS performance at different temperatures employing different photon flux values. Thus, for the evaluation of the photocatalytic activities at different VIS flux values (*i.e.* at different temperatures), photocatalytic NO_x storage and NO₂ generation were normalized with the incident VIS photon flux values and presented in terms of corresponding

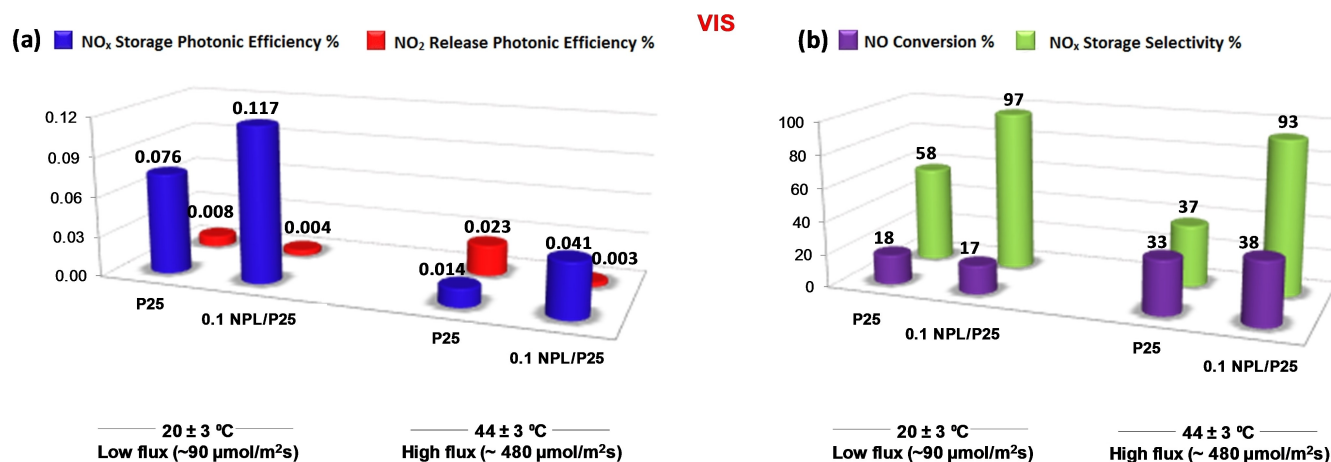


Figure 12. Temperature-dependent PHONOS data for pure P25 and 0.1NPL/P25 under VIS-light illumination (a) NO_x storage photonic efficiency % and NO₂ release photonic efficiency %, (b) NO conversion % and NO_x storage selectivity % values.

photonic efficiency % values, as shown in Figure 12a. As a comparison, corresponding NO conversion % and NO_x storage % data are also provided in Figure 12b.

These results clearly demonstrate that increasing temperature during VIS-light illumination tends to decline the NO_x storage photonic efficiency % of pure P25 possibly due to accelerated electron-hole recombination or increased water dissociation and poisoning of the titania surface with an extensive amount of adsorbed hydroxyl/hydroxide species.

In the case of 0.1NPL/P25, while increasing temperature has almost no effect on NO₂ release photonic efficiency %, it drastically diminishes the NO_x storage photonic efficiency %, again suggesting a decrease in overall PHONOS performance with increasing temperature. Therefore, both of the control experiments presented in Figure 12a indicate that an increase in the reactor temperature during the VIS-light illumination cannot be responsible for the observed boost in photocatalytic activity, depicted in Figure 9 and the photocatalytic enhancement observed for the NPL/P25 composite system is a result of photocatalytic routes rather than conventional thermal catalytic routes.

Conclusions

In this work, oleic acid functionalized CdSe/CdSeTe core/crown nanoplatelets were incorporated to titania (P25) and the synthesized composites were successfully utilized in photocatalytic NO_x oxidation and storage (PHONOS) under both UV-A and VIS-light illumination. The proposed NPL/P25 composite photocatalysts with optimized NPL loadings displayed a relatively high NO (g) conversion and extremely high selectivity toward NO_x storage as compared to the commercial P25 titania benchmark photocatalyst both under UV-A and VIS-illumination. Through a series of comprehensive control experiments, roles of the individual components of the NPL/P25 composite were identified. These experiments demonstrated that NPL/P25 composite outperformed the individual functionalities in their separated forms. It was shown that while primary photocatalytic active sites for NO oxidation reside on titania, NPL provided a synergistic boost both in NO conversion as well as NO_x storage selectivity. The origin of the enhanced NO conversion can be attributed to the presumably improved electron-hole separation capability of the utilized colloidal quantum wells. Having Type-II band alignment, the electron and hole wave functions are possibly positioned in different parts of the NPL heterostructure, resulting in spatial separation of charge carriers and longer fluorescence lifetimes. Furthermore, oleic acid functionalities as well as CdSe/CdSeTe core/crown nanoplatelets also facilitated NO₂ adsorption, extended the surface residence time of adsorbed NO₂ species and assisted their conversion to nitrates. Control experiments revealed that toluene (C₆H₅CH₃ (l)) used as the dispersing medium for NPL also provided a relatively small boost in NO conversion, however this effect disappeared upon extended operational durations due to the photocatalytic/photochemical degradation of adsorbed toluene. NPL/P25 systems revealed reasonable reusability under VIS illumination,

while reusability was limited under UV-A illumination. Attenuation of the PHONOS performance upon photochemical aging and extended operation can be linked to electronic changes in the Cd species as well as degradation of the oleic acid capping of the NPL system. Influence of temperature was also studied for the PHONOS performance of NPL/P25 composites under VIS-light suggesting a decrease in photocatalytic efficiency with increasing temperature due to the possible increase in electron-hole recombination rate and the increased formation of hydroxide/hydroxyl surface functionalities poisoning the photocatalyst surface. Similar NPL/P25-based composite systems can be used as a new family of active photocatalytic materials with a significant potential in various environmental remediation and solar energy conversion applications.

Experimental Section

Cadmium nitrate tetrahydrate (Cd(NO₃)₂·4H₂O; 99% trace metal basis), cadmium acetate dihydrate (Cd(OAc)₂·2H₂O; 98%), sodium myristate (CH₃(CH₂)₁₂COONa, ≥ 99%), titanium (IV) oxide (P25, ≥ 99.5% trace metal basis), 1-octadecene (ODE, technical grade), tellurium (Te), selenium (Se), oleic acid (OA, 90% technical grade), trioctylphosphine (TOP), hexane, ethanol, methanol and toluene were purchased from Sigma Aldrich and used as received without further purification.

Synthesis of CdSe(core)/CdSeTe (crown) nanoplatelets

Synthesis of cadmium myristate

Cadmium myristate (C₂₈H₅₄CdO₄, Cd(II) tetradecanoate) was prepared according to our previously published protocol with slight modifications.^[89] In a typical synthesis, 6.26 g of sodium myristate and 2.46 g of cadmium nitrate tetrahydrate were separately dissolved in 500 and 80 mL of methanol, respectively. Upon complete dissolution, the solutions were mixed and stirred vigorously for 3 h. Consequently, the white cadmium myristate powder was precipitated by centrifugation and washed with methanol three times to remove any unwanted impurities and/or side products. Lastly, cadmium myristate was dried overnight under vacuum at room temperature (RT).

Synthesis of CdSe core of NPL

CdSe core of NPL having a four-monolayer (4 ML, *i.e.* consisting of four Se atomic layers and five Cd atomic layers) thickness were synthesized by using a former procedure discussed elsewhere.^[50,90] Along these lines, 20 mg of Se, 340 mg of cadmium myristate (synthesized in previous step) and 30 mL of 1-octadecene were placed in a 100 mL three-neck flask and degassed at 95 °C for 1 h to remove oxygen, water and any other volatile species. Next, the sample temperature was increased under the Ar(g) flow. At *ca.* 195 °C, the color of the reaction solution turned golden yellow, after which 120 mg of Cd (OAc)₂·2H₂O was promptly added to the reaction system. After having kept the reaction solution at 240 °C for 8 min for further growth of NPL, 1 mL of oleic acid was injected. At this point, reaction was stopped, and the temperature of the solution was brought to room temperature. Subsequently, hexane (10 mL) and ethanol (10 mL) were added to the solution to precipitate the synthesized NPL. Finally, NPL were centrifuged and stored in hexane for the crown coating step.

Synthesis of the 4 ML-Thick CdSe/CdSe_{0.75}Te_{0.25} core/alloyed crown

For a typical synthesis,^[55] 2 mL of 4 ML-thick CdSe core suspension in hexane (where 0.1 mL of this suspension in 3 mL of hexane had an optical density of 0.9 at 512 nm), 10 mL of 1-octadecene, 100 μ L of oleic acid and 50 mg of cadmium acetate dihydrate were combined in a 25 mL three-neck round bottom flask. The reaction mixture was degassed at RT for 1 h and then was set to 215 °C under Ar (g) flow for the growth of the CdTe crown region. At 185 °C, 0.75 mL of ODE-TOP-Se-Te solution was injected to the reaction medium at a rate of 2.5 mL/h (where ODE-TOP-Se-Te solution was prepared by mixing 79 mg Se and 127.6 mg Te with 2 mL of TOP in an inert atmosphere overnight to ensure complete dissolution. Next, 60 μ L of this mixture was diluted with 2 mL of ODE to achieve the final ODE-TOP-Se-Te solution). It is important to note here that, if needed, the size of the crown region could be controlled by varying the amount of the injected ODE-TOP-Se-Te solution. Immediately after the injection of ODE-TOP-Se-Te solution, 1 mL of oleic acid was swiftly added to the reaction medium and the solution was quenched to RT. CdSe/CdSe_{0.75}Te_{0.25} core/alloyed crown NPL were precipitated by the addition of ethanol, centrifuged and finally dispersed in toluene for further studies.

Preparation of CdSe/CdSe_{0.75}Te_{0.25}/P25 composite materials

To synthesize CdSe/ CdSe_{0.75}Te_{0.25}/P25 composite systems, different volumes of CdSe/ CdSe_{0.75}Te_{0.25} NPL colloidal suspensions in toluene were drop cast on 250 mg of P25 (*i. e.* TiO₂). After physical mixing of the NPL with P25 for 2 min, samples were dried in an oven at 70 °C for 18 h. The samples were labeled as 0.05NPL/P25, 0.1NPL/P25, 0.5NPL/P25, 1.0NPL/P25, 2.0NPL/P25, and 6.0NPL/P25, where the numbers in the left-hand side of the acronyms represent the corresponding volume (mL) of NPL loading on P25. Furthermore, additional samples were also prepared in order to elucidate the effect of toluene (*i. e.* NPL dispersing medium) on the photocatalytic performance of P25. For this purpose, various amounts of toluene were drop-cast on P25 at RT followed by evaporation and drying at 70 °C for 18 h. These samples are designated as XT/P25, where X represents the volume of toluene dosed on P25 in mL (*i. e.* X=0.1, 0.5, or 2.0 mL).

Structural characterization Methods

Crystallographic structures of the synthesized materials were determined by using a PANalytical Empyrean XRD diffractometer equipped with Cu K α irradiation source. (40 kV, 45 mA, λ =1.5405 Å). Transmission electron microscopy (TEM), scanning transmission electron microscopy (STEM), high-angle annular dark field (HAADF) imaging and energy dispersive X-ray (EDX) analysis experiments were carried out at 120 kV using a Hitachi High-tech HT7700 TEM equipped with BF-/DF-STEM-EDX modules at DAYTAM user facility (Ataturk University, Erzurum, Turkey). X-ray photoelectron spectroscopy (XPS) experiments were performed with a SPECS PHOIBOS hemispherical energy analyzer. A monochromatic Al-K α X-ray excitation source (14 kV, 350 W) was employed during the XPS data acquisition. BET specific surface area (SSA) measurements of the synthesized catalysts were determined by using nitrogen adsorption-desorption isotherms obtained with a Micromeritics 3Flex surface area and pore size analyzer. Prior to SSA analysis, all samples were outgassed in vacuum for 2 h at 150 °C. UV-VIS absorption spectra were obtained using an UV-VIS-NIR Spectrometer-Cary 5000-and toluene (*i. e.* dispersing medium) was used as a reference. The photoluminescence (PL) spectra were acquired at room temperature using a Jobin-Yvon Horiba Fluorolog-3 spectrometer equipped with a Hamamatsu R928 P detector and a 450W

ozone-free Osram XBO xenon arc lamp. The excitation wavelength was 400 nm (*i. e.* 3.1 eV), which is well above the band gap of NPL. The fluorescence was monitored at a right angle relative to the excitation. Electron paramagnetic resonance (EPR) measurements were performed with a Bruker EMX Nano spectrometer with an integrated referencing for g-factor calculation and also integrated spin counting units. The microwave frequency of the cavity was 9.41 GHz (X-band) and all spectra were measured at RT with 0.1 mT modulation amplitude, 2 mW microwave power and 120 scans (sweep time 60 s/scan, time constant 81.92 ms). Before the measurements, EPR samples were inserted into a spin-free 25 cm long quartz tube (Qsil[®], Germany). *In-situ* EPR experiments were also carried out in the presence of UV-light irradiation using an ER 203 UV radiation system containing a short-arc mercury lamp (LSB 610 100W Hg, LOT-Quantum Design).

Photocatalytic activity measurements

The photocatalytic NO_x oxidation and storage performance measurements were executed at RT in a custom-designed flow reactor by considering the experimental requirements reported in the ISO 22197-1 standard.^[91] Inlet gas mixture introduced to the reactor (Figure S9) contained 0.750 standard liters per minute (SLM) N₂ (g) (purity: 99.99%, Linde GmbH), 0.250 SLM O₂ (g) (purity: 99%, Linde GmbH) and 0.01 SLM NO (g) (100 ppm NO (g) diluted in balance N₂ (g), Linde GmbH). To obtain gas flow values mentioned above, mass flow controllers (MKS 1479 A for N₂ (g) and Teledyne HFC-202 for NO (g) diluted in N₂ (g)) were utilized so that the total gas flow over the photocatalyst was kept at 1.010 SLM \pm 0.05 SLM, where the NO (g) content of the inlet gas mixture was fixed at 1.00 ppm. The pressure inside the reactor was kept at *ca.* 1 bar and measured with an MKS Baratron 622B capacitance manometer. Humidity of the inlet gas mixture was also carefully controlled by dosing varying amounts of water vapor into the inlet gas mixture (*i. e.* before the reactor entrance) with the help of PermSelect (PDMSXA-2500) semipermeable membrane module attached to an external variable-temperature water chiller/recycler. Typical relative humidity of the reactor was kept within 50 \pm 3% at 23 \pm 2 °C, measured at the sample position using a Hanna HI 9565 humidity analyzer. The changes in the total NO_x, NO and NO₂ concentrations at the reactor outlet were monitored *via* a chemiluminescent NO_x analyzer (Horiba APNA-370) with a 0.1 ppb sensitivity and 1 Hz data acquisition speed. For the experiments performed with UV-A irradiation, an 8W UV-A lamp (F8W/T5/BL350, Sylvania, Germany) was used, while for the experiments carried out with VIS light illumination, a 35W metal halide lamp (HCI-TC 35W/942 NDL PB 400–700 nm range, OSRAM) was utilized. Since the utilized VIS light source also emitted a limited but detectable flux of UV-A light, a commercial VIS transparent UV-A-blocker/filtering film (LLumar window film UV-A CL SR PS (clear)) was placed on top of the reactor during the VIS-light experiments. This was crucial for ruling out any contribution from UV-A photons during the VIS-light illumination. The incoming light flux was measured carefully before and after each UV-A and VIS-light measurement with a photo radiometer (HD2302.0, Delta Ohm/Italy) using a UV-A probe (315–400 nm) and a PAR VIS probe (400–700 nm), respectively. Typical VIS-light photon flux values used in the current experiments were within 450–500 μ mol/(m².s), while typical UV-A-light power density values were within 7.7–8.3 W/m². Note that the photon flux of the VIS light source was about 15 times greater than that of the UV-A light source. Relative percentile of VIS photon flux in typical solar radiation is also significantly greater than that of UV-A photon flux (*i. e.*, *ca.* 42% VIS vs. 6% UV-A). Reactor temperature remained within 23 \pm 2 °C during UV-A measurements, whereas during VIS light experiments, the reactor temperature reached up to 46 °C after a typical 60 min photocatalytic activity test. In each perform-

ance analysis test, 250 mg of photocatalyst was packed in a 2 mm × 40 mm × 40 mm polymethyl methacrylate (PMMA) sample holder and placed into the flow reactor. To quantify the photocatalytic activity and selectivity, at the end of a typical 1 h photocatalytic activity test, obtained raw data was processed in order to obtain various figures of merit (such as % photonic efficiency towards NO_x storage, % photonic efficiency for NO₂ generation, % NO conversion, % selectivity towards NO_x storage, and DeNO_x index). Numerical definitions of these figures of merit are provided in the Supporting Information (SI) section.

Acknowledgements

EO, EE, MI acknowledge the financial support from the Scientific and Technological Research Council of Turkey (TUBITAK) (Project Code: 116M435). EO acknowledges the scientific collaboration with TARLA project founded by the Ministry of Development of Turkey (project code: DPT2006K-120470). HVD gratefully acknowledge support from TÜBA. Authors also acknowledge Mr. Mete Duman (UNAM- National Nanotechnology Center) for the design of technical graphics.

Conflict of Interest

The authors declare no conflict of interest.

Keywords: Photocatalytic NO_x abatement · PHONOS, DeNO_x, titanium dioxide · CdSe/CdSeTe nanoplatelets · quantum-wells

- [1] K. Skalska, J. S. Miller, S. Ledakowicz, *Sci. Total Environ.* **2010**, *408*, 3976–3989.
- [2] A. Folli, S. B. Campbell, J. A. Anderson, D. E. Macphree, *J. Photochem. Photobiol. A* **2011**, *220*, 85–93.
- [3] S. Roy, M. S. Hegde, G. Madras, *Appl. Energy* **2009**, *86*, 2283–2297.
- [4] Z. Say, O. Mihai, M. Kurt, L. Olsson, E. Ozensoy, *Catal. Today* **2019**, *320*, 152–164.
- [5] Z. Say, M. Tohumeken, E. Ozensoy, *Catal. Today* **2014**, *231*, 135–144.
- [6] S. M. Andonova, G. S. Senturk, E. Ozensoy, *J. Phys. Chem. C* **2010**, *114*, 17003–17016.
- [7] P. Granger, V. I. Parvulescu, *Chem. Rev.* **2011**, *111*, 3155–3207.
- [8] J. C. Schlatter, P. J. Mitchell, *Ind. Eng. Chem. Prod. Res. Dev.* **1980**, *19*, 288–293.
- [9] G. Djéga-Mariadassou, M. Berger, O. Gorce, J. W. Park, H. Pernot, C. Potvin, C. Thomas, P. Da Costa, *Elsevier*. **2007**, 145–173.
- [10] J. Gong, D. Wang, J. Li, K. Kamasamudram, N. Currier, A. Yezerets, *Catal. Today* **2019**, *320*, 51–60.
- [11] G. P. Chossière, R. Malina, F. Allroggen, S. D. Eastham, R. L. Speth, S. R. Barret, *Atmos. Environ.* **2018**, *189*, 89–97.
- [12] F. Parrino, C. De Pasquale, L. Palmisano, *ChemSusChem* **2019**, *12*, 589–602.
- [13] J. Patzsch, J. N. Spencer, A. Folli, J. Z. Bloh, *RSC Adv.* **2018**, *8*, 27674–27685.
- [14] M. Balci Leinen, D. Dede, M. U. Khan, M. Çağlayan, Y. Koçak, H. V. Demir, E. Ozensoy, *ACS Appl. Mater. Interfaces* **2019**, *11*, 865–879.
- [15] K. Fujiwara, S. E. Pratsinis, *Appl. Catal. B* **2018**, *226*, 127–134.
- [16] N. O. Balayeva, M. Fleisch, D. W. Bahnemann, *Catal. Today* **2018**, *313*, 63–71.
- [17] W. G. Lu, A. D. Olaitan, M. R. Brantley, B. Zekavat, D. A. Erdogan, E. Ozensoy, T. Solouki, *J. Phys. Chem. C* **2016**, *120*, 8056–8067.
- [18] M. Çağlayan, M. Irfan, K. E. Ercan, Y. Kocak, E. Ozensoy, *Appl. Catal. B* **2020**, *263*, 118227.
- [19] J. Angelo, L. Andrade, A. Mendes, *Appl. Catal. A* **2014**, *484*, 17–25.
- [20] R. Sugraney, J. I. Alvarez, M. Cruz-Yusta, I. Marmol, J. Morales, J. Vila, L. Sanchez, *Build. Environ.* **2013**, *69*, 55–63.
- [21] C. Guo, X. Wu, M. Yan, Q. Dong, S. Yin, T. Sato, S. Liu, *Nanoscale* **2013**, *5*, 8184–8191.
- [22] M. M. Ballari, H. J. H. Brouwers, *J. Hazard. Mater.* **2013**, *254–255*, 406–414.
- [23] H. Chen, C. E. Nanayakkara, V. H. Grassian, *Chem. Rev.* **2012**, *112*, 5919–5948.
- [24] J. Schneider, M. Matsuoka, M. Takeuchi, J. Zhang, Y. Horiuchi, M. Anpo, D. W. Bahnemann, *Chem. Rev.* **2014**, *114*, 9919–9986.
- [25] R. Daghrir, P. Drogui, D. Robert, *Ind. Eng. Chem. Res.* **2013**, *52*, 3581–3599.
- [26] H. Zhang, J. F. Banfield, *Chem. Rev.* **2014**, *114*, 9613–9644.
- [27] M. Pelaez, N. T. Nolan, S. C. Pillai, M. K. Seery, P. Falaras, A. G. Kontos, P. S. M. Dunlop, J. W. J. Hamilton, J. A. Byrne, K. O'Shea, M. H. Entezari, D. D. Dionysiou, *Appl. Catal., B* **2012**, *125*, 331–349.
- [28] S. Jafari, M. R. Mohammadi, H. R. M. Hosseini, *Ind. Eng. Chem. Res.* **2016**, *55*, 12205–12212.
- [29] J. Z. Ma, H. M. Wu, Y. C. Liu, H. He, *J. Phys. Chem. C* **2014**, *118*, 7434–7441.
- [30] X. Chen, L. Liu, P. Y. Yu, S. S. Mao, *Science* **2011**, *331*, 746–751.
- [31] M. Sugrañez, J. Balbuena, M. Cruz-Yusta, F. Martín, J. Morales, L. Sánchez, *Appl. Catal., B* **2015**, *165*, 529–536.
- [32] L. Kong, C. Wang, F. Wan, H. Zheng, X. Zhang, *Appl. Surf. Sci.* **2017**, *396*, 26–35.
- [33] Y. Y. Duan, J. M. Luo, S. C. Zhou, X. Y. Mao, M. W. Shah, F. Wang, Z. H. Chen, C. Y. Wang, *Appl. Catal., B* **2018**, *234*, 206–212.
- [34] Y. Hu, X. Song, S. M. Jiang, C. H. Wei, *Chem. Eng. J.* **2015**, *274*, 102–112.
- [35] Z. Shi, L. Lan, Y. Li, Y. Yang, Q. Zhang, J. Wu, G. Zhang, X. Zhao, *ACS Sustain. Chem. Eng.* **2018**, *6*, 16503–16514.
- [36] A. Martinez-Oviedo, S. K. Ray, H. P. Nguyen, S. W. Lee, *J. Photochem. Photobiol., A* **2019**, *370*, 18–25.
- [37] P. Wang, D. Z. Li, J. Chen, X. Y. Zhang, J. J. Xian, X. Yang, X. Z. Zheng, X. F. Li, Y. Shao, *Appl. Catal., B* **2014**, *160*, 217–226.
- [38] Y. X. Zhu, Y. F. Wang, Z. Chen, L. S. Qin, L. B. Yang, L. Zhu, P. Tang, T. Gao, Y. X. Huang, Z. L. Sha, G. Tang, *Appl. Catal., A* **2015**, *498*, 159–166.
- [39] W. Gao, M. Wang, C. Ran, L. Li, *Chem. Commun* **2015**, *51*, 1709–1712.
- [40] X. Y. Li, D. S. Wang, G. X. Cheng, Q. Z. Luo, J. An, Y. H. Wang, *Appl. Catal., B* **2008**, *81*, 267–273.
- [41] Q. L. Yu, M. M. Ballari, H. J. H. Brouwers, *Appl. Catal., B* **2010**, *99*, 58–65.
- [42] J. Z. Bloh, A. Folli, D. E. Macphree, *RSC Adv.* **2014**, *4*, 45726–45734.
- [43] S. Ithurria, M. D. Tessier, B. Mahler, R. P. S. M. Lobo, B. Dubertret, A. L. Efros, *Nat. Mater.* **2011**, *10*, 936–941.
- [44] E. Lhuillier, S. Pedetti, S. Ithurria, B. Nadal, H. Heuclin, B. Dubertret, *Acc. Chem. Res.* **2015**, *48*, 22–30.
- [45] A. Yeltik, S. Delikanli, M. Olutas, Y. Kelestemur, B. Guzelurk, H. V. Demir, *J. Phys. Chem. C* **2015**, *119*, 26768–26775.
- [46] L. T. Kunnehan, M. D. Tessier, H. Heuclin, B. Dubertret, Y. V. Aulin, F. C. Grozema, J. M. Schins, L. D. A. Siebbeles, *T. J. Phys. Chem. Lett.* **2013**, *4*, 3574–3578.
- [47] A. Brumberg, B. T. Diroll, G. Nedelcu, M. E. Sykes, Y. Liu, S. M. Harvey, M. R. Wasielewski, M. V. Kovalenko, R. D. Schaller, *Nano Lett.* **2018**, *18*, 4771–4776.
- [48] M. Olutas, B. Guzelurk, Y. Kelestemur, A. Yeltik, S. Delikanli, H. V. Demir, *ACS Nano* **2015**, *9*, 5041–5050.
- [49] S. Pedetti, B. Nadal, E. Lhuillier, B. Mahler, C. Bouet, B. Abécassis, B. Dubertret, *Chem. Mater.* **2013**, *25*, 2455–2462.
- [50] M. D. Tessier, P. Spinicelli, D. Dupont, G. Patriarche, S. Ithurria, B. Dubertret, *Nano Lett.* **2014**, *14*, 207–213.
- [51] B. Mahler, B. Nadal, C. Bouet, G. Patriarche, B. Dubertret, *J. Am. Chem. Soc.* **2012**, *134*, 18591–18598.
- [52] Y. Kelestemur, B. Guzelurk, O. Erdem, M. Olutas, K. Gungor, H. V. Demir, *Adv. Funct. Mater.* **2016**, *26*, 3570–3579.
- [53] D. Dorfs, T. Franzl, R. Osovsky, M. Brumer, E. Lifshitz, T. A. Klar, A. Eychemuller, *Small* **2008**, *4*, 1148–1152.
- [54] S. Pedetti, S. Ithurria, H. Heuclin, G. Patriarche, B. Dubertret, *J. Am. Chem. Soc.* **2014**, *136*, 16430–16438.
- [55] Y. Kelestemur, M. Olutas, S. Delikanli, B. Guzelurk, M. Z. Akgul, H. V. Demir, *J. Phys. Chem. C* **2015**, *119*, 2177–2185.
- [56] K. Wu, Q. Li, Y. Jia, J. R. McBride, Z. X. Xie, T. Lian, *ACS Nano* **2015**, *9*, 961–968.
- [57] J. Hensel, G. Wang, Y. Li, J. Z. Zhang, *Nano Lett.* **2010**, *10*, 478–483.
- [58] B. Bajorowicz, J. Nadolna, W. Lisowski, T. Klimczuk, A. Zaleska-Medynska, *Appl. Catal., B* **2017**, *203*, 452–464.

- [59] A. A. Mosquera, D. Horwat, A. Rashkovskiy, A. Kovalev, P. Miska, D. Wainstein, J. M. Albella, J. L. J. S. r. Endrino, *Sci. Rep.* **2013**, *3*, 1714.
- [60] S. Bourgeois, P. Leseigneur, M. Perdereau, *Surf. Sci.* **1995**, *328*, 105–110.
- [61] H. S. White, A. J. Ricco, M. S. Wrighton, *J. Phys. Chem.* **1983**, *87*, 5140–5150.
- [62] G. R. Bhand, N. B. Chaure, *Mater. Sci. Semicond. Process.* **2017**, *68*, 279–287.
- [63] A. P. Kumar, B. T. Huy, B. P. Kumar, J. H. Kim, V. D. Dao, H. S. Choi, Y. I. Lee, *J. Mater. Chem. C* **2015**, *3*, 1957–1964.
- [64] M. N. Ghazzal, R. Wojcieszak, G. Raj, E. M. Gaigneaux, *Beilstein J. Nanotechnol.* **2014**, *5*, 68–76.
- [65] B. Guzelturk, Y. Kelestemur, M. Olutas, Q. Li, T. Lian, H. V. Demir, *J. Phys. Chem. Lett.* **2017**, *8*, 5317–5324.
- [66] Y. Wang, Q. Wang, X. Zhan, F. Wang, M. Safdar, J. He, *Nanoscale* **2013**, *5*, 8326–8339.
- [67] M. A. Mumin, G. Moula, P. A. Charpentier, *RSC Adv.* **2015**, *5*, 67767–67779.
- [68] H. T. Tung, D. Van Thuan, J. H. Kiat, D. H. Phuc, *Appl. Phys. A* **2019**, *125*, 505
- [69] A. Hassanien, A. A. Akl, *Superlattices Microstruct.* **2016**, *89*, 153–169.
- [70] O. I. Mičić, A. J. Nozik, E. Lifshitz, T. Rajh, O. G. Poluektov, M. C. Thurnauer, *J. Phys. Chem. B* **2002**, *106*, 4390–4395.
- [71] M. Jones, S. S. Lo, G. D. Scholes, *Proc. Natl. Acad. Sci. U. S. A.* **2009**, *106*, 3011–3016.
- [72] G. Bačić, A. Pavičević, F. Peyrot, *Redox Biol.* **2016**, *8*, 226–242.
- [73] D. R. Cooper, N. M. Dimitrijevic, J. L. Nadeau, *Nanoscale* **2010**, *2*, 114–121.
- [74] S. M. Goodman, M. Levy, F.-F. Li, Y. Ding, C. M. Courtney, P. P. Chowdhury, A. Erbse, A. Chatterjee, P. Nagpal, *Front. Chem.* **2018**, *6*, 46.
- [75] R. Strassberg, S. Delikanli, Y. Barak, J. Dehnel, A. Kostadinov, G. Maikov, P. L. Hernandez-Martinez, M. Sharma, H. V. Demir, E. Lifshitz, *J. Phys. Chem. Lett.* **2019**, *10*, 4437–4447.
- [76] V. Ramachandran, J. van Tol, A. M. McKenna, R. P. Rodgers, A. G. Marshall, N. S. Dalal, *Anal. Chem.* **2015**, *87*, 2306–2313.
- [77] I. R. Macdonald, S. Rhydderch, E. Holt, N. Grant, J. M. Storey, R. F. Howe, *Catal. Today* **2012**, *182*, 39–45.
- [78] S. M. Andonova, G. S. Şentürk, E. Kayhan, E. Ozensoy, *J. Phys. Chem. C* **2009**, *113*, 11014–11026.
- [79] J. Patzsch, A. Folli, D. E. Macphee, J. Z. Bloh, *Phys. Chem. Chem. Phys.* **2017**, *19*, 32678–32686.
- [80] O. Carp, C. L. Huisman, A. Reller, *Prog. Solid State Chem.* **2004**, *32*, 33–177.
- [81] L. Sivachandiran, F. Thevenet, P. Gravejat, A. Rousseau, *Appl. Catal., B* **2013**, *142*, 196–204.
- [82] L. Yang, A. Hakkı, F. Wang, D. E. Macphee, *ACS Appl. Mater. Interfaces* **2017**, *9*, 17034–17041.
- [83] R. Dillert, A. Engel, J. Grosse, P. Lindner, D. W. Bahnemann, *Phys. Chem. Chem. Phys.* **2013**, *15*, 20876–20886.
- [84] J. Freitag, A. Dominguez, T. A. Niehaus, A. Hulsewig, R. Dillert, T. Frauenheim, D. W. Bahnemann, *J. Phys. Chem. C* **2015**, *119*, 4488–4501.
- [85] Y. Ohko, Y. Nakamura, N. Negishi, S. Matsuzawa, K. Takeuchi, *J. Photochem. Photobiol., A* **2009**, *205*, 28–33.
- [86] Y. Ohko, Y. Nakamura, N. Negishi, S. Matsuzawa, K. J. E. C. L. Takeuchi, *Environ. Chem. Lett.* **2010**, *8*, 289–294.
- [87] J. Rathouský, V. Kalousek, M. Kolář, J. Jirkovský, P. Barták, *Catal. Today* **2011**, *161*, 202–208.
- [88] S. Ardizzone, C. L. Bianchi, G. Cappelletti, A. Naldoni, C. Pirola, *Environ. Sci. Technol.* **2008**, *42*, 6671–6676.
- [89] Y. Kelestemur, B. Guzelturk, O. Erdem, M. Olutas, T. Erdem, C. F. Usanmaz, K. Gungor, H. V. Demir, *J. Phys. Chem. C* **2017**, *121*, 4650–4658.
- [90] Y. Altintas, U. Quliyeva, K. Gungor, O. Erdem, Y. Kelestemur, E. Mutlugun, M. V. Kovalenko, H. V. Demir, *Small* **2019**, *15*, 8, 1804854.
- [91] ISO 22197–1. *I. O.f.Standardization*. **2007**, 1–11.

Manuscript received: May 1, 2020

Revised manuscript received: September 17, 2020

Accepted manuscript online: September 22, 2020

Version of record online: October 27, 2020